Mon. Not. R. Astron. Soc. **000**, 000–000 (0000) Printed 12 April 2012 (MN LATEX style file v2.2)

# Measuring mass-loss rates and constraining shock physics using X-ray line profiles of O stars from the *Chandra* archive

David H. Cohen,[1⋆] Emma E. Wollman,[1,2] Maurice A. Leutenegger,[3,4]
Jon O. Sundqvist,[5] Alex W. Fullerton,[6] Janos Zsargó[7] Stanley P. Owocki[5]
[1] *Swarthmore College, Department of Physics and Astronomy, Swarthmore, Pennsylvania 19081, USA*
[2] *Caltech, Department of Physics, 1200 East California Blvd., Pasadena, California 91125, USA*
[3] *NASA/Goddard Space Flight Center, Code 662, Greenbelt, Maryland 20771, USA*
[4] *CRESST and University of Maryland, Baltimore County, MD 21250, USA*
[5] *University of Delaware, Bartol Research Institute, Newark, Delaware 19716, USA*
[6] *Space Telescope Science Institute, 3700 San Martin Dr., Baltimore, Maryland 21218, USA*
[7] *Instituto Politécnico Nacional, Escuela Superior de Fisica y Matemáticas, C.P. 07738, Mexico, D.F., Mexico*

12 April 2012

**ABSTRACT**

We quantitatively investigate the extent of wind absorption signatures in the X-ray grating spectra of all non-magnetic, effectively single O stars in the *Chandra* archive via line-profile fitting. Under the usual assumption of a spherically symmetric wind with embedded shocks, we confirm previous claims that some objects show little or no wind absorption. However, other objects do show asymmetric and blue shifted line profiles, indicative of wind absorption. For these stars, we are able to derive wind mass-loss rates from the ensemble of line profiles, and find values modestly lower than theory predicts, and consistent with H$\alpha$ if clumping factors of $f_{cl} \approx 20$ are assumed. The same profile fitting indicates an onset radius of X-rays typically at $r \approx 1.5\ R_*$, and terminal velocities for the X-ray emitting wind component that are consistent with that of the bulk wind. Both of these results are in agreement with the predictions of numerical simulations of embedded wind shocks due to the line-driving instability. We explore the likelihood that the stars in the sample that do not show significant wind absorption signatures in their line profiles have at least some X-ray emission that arises from colliding wind shocks with a close binary companion.

**Key words:** stars: early-type – stars: mass-loss – stars: winds, outflows – X-rays: stars

## 1 INTRODUCTION

By losing mass at a rate of $\dot{M} \sim 10^{-6}\ M_\odot\ yr^{-1}$ via its stellar wind, an O star can shed a significant portion of its mass over the course of its lifetime. This continuous loss of mass transfers energy and momentum to the surrounding interstellar medium and can significantly reduce the mass of a core-collapse supernova progenitor. So, the wind mass-loss rate is an important parameter in the study of both stellar evolution and of the Galactic environment. In recent years there has been increased awareness of large systematic uncertainties in many mass-loss rate diagnostics, primarily due to wind clumping, rendering the actual mass-loss rates of O stars somewhat controversial (e.g. Hamann et al. (2008)).

X-rays provide a potentially good clumping-insensitive mass-loss rate diagnostic via the effect of wind attenuation on X-ray emission line profile shapes. The characteristic line profile shape that provides the diagnostic power arises because red-shifted photons emitted from the rear hemisphere of the wind are subject to more attenuation than the blue-shifted photons originating in the front hemisphere (see figure 2 in Cohen et al. (2010)). The degree of blue shift and asymmetry in these line profiles is then directly proportional to the wind column density and thus to the mass-loss rate. By fitting a simple quantitative model (Owocki & Cohen 2001) to each emission line in a star's spectrum and then analyzing the ensemble of lines, we can determine the star's mass-loss rate (Cohen et al. 2010, 2011).

Because this diagnostic scales with the column density rather than the square of the density, it avoids many of the problems presented by traditional mass-loss rate diagnostics. In particular, density-squared diagnostics such as H$\alpha$ and

⋆ E-mail: cohen@astro.swarthmore.edu

radio or IR free-free emission will overestimate the mass-loss rate if clumping is not accounted for. And even when clumping is accounted for, there is a degeneracy between the mass-loss rate and the clumping factor. UV absorption line diagnostics are sensitive to ionization corrections which are highly uncertain and also are subject to density-squared clumping effects. Recent, more sophisticated application of these diagnostics, assuming a radially dependent clumping factor, has led to a downward revision of the mass-loss rates of O stars (Bouret et al. 2005; Fullerton et al. 2006; Puls et al. 2006). These lowered mass-loss rates provide a natural explanation for the initially surprising discovery (Kahn et al. 2001; Cassinelli et al. 2001) that X-ray line profiles are not as symmetric as traditional mass-loss rate estimates had implied.

While small-scale, optically thin clumping reconciles the X-ray, UV, H$\alpha$, IR, and radio data for these stars, there is no direct evidence for large-scale, optically thick clumping, or porosity, in the X-ray data themselves (Cohen et al. 2008; Sundqvist et al. 2012; Leutenegger et al. 2012). Porosity results from optically thick clumps, which can "hide" opacity in their interiors. While porosity has been proposed as an explanation for the more-symmetric-than-expected X-ray line profiles (Oskinova et al. 2006), very large porosity lengths are required in order for porosity to have any effect on line profiles (Owocki & Cohen 2006), and levels of porosity consistent with measured line profiles produce only modest ($\sim$ 25 per cent) effects on derived mass-loss rates (Sundqvist et al. 2012; Leutenegger et al. 2012). In this paper, we derive mass-loss rates from the measured X-ray line profiles under the assumption that significant porosity is not present. *Co-authors: I'm not sure this paragraph belongs here in the intro. We could wait till the discussion to talk about porosity at all. What do you think?*

The initial application of our X-ray line profile based mass-loss rate diagnostic to the O supergiant $\zeta$ Pup gave a mass-loss rate of $\dot{M} = 3.5 \times 10^{-6}$ M$_\odot$ yr$^{-1}$ (Cohen et al. 2010). This represents a factor of three reduction over the unclumped H$\alpha$ value (Repolust et al. 2004; Puls et al. 2006), and is consistent with the newer analysis of H$\alpha$, IR, and radio data which sets an upper limit of $\dot{M} < 4.2 \times 10^{-6}$ M$_\odot$ yr$^{-1}$ when the effects of clumping are accounted for (Puls et al. 2006). A similar reduction is found for the very early O supergiant, HD 93129A, where the X-ray mass-loss rate of $\dot{M} = 7 \times 10^{-6}$ M$_\odot$ yr$^{-1}$ is consistent with the observed H$\alpha$ line if clumping is accounted for via $f_{cl} = 12$ (Cohen et al. 2011).

The goal of this paper is to extend the X-ray line-profile mass-loss rate analysis to all the non-magnetic, effectively single[1] O stars with grating spectra in the *Chandra* archive. It is already known that some, especially later-type, O stars show no obvious wind attenuation signatures (Miller et al. 2002; Skinner et al. 2008), and as one looks toward weaker winds in early B stars, the X-ray lines are not as broad as the wind velocities would suggest they should be (Cohen et al. 2008). Therefore, we have excluded from our sample very late-O main sequence stars with relatively narrow lines, but we do include late-O giants and supergiants, even when the profiles appear unaffected by attenuation. In these cases we want to quantify the level of attenuation that may be hidden in the noise, placing upper limits on their mass-loss rates. Of course, it is possible that the model assumptions break down for some of the stars in the sample, not least of all if wind-wind interactions with a binary companion is responsible for some of the X-ray emission, in which case an intrinsically symmetric emission line profile may dilute whatever attenuation signal is present.

An additional goal of this paper is to constrain wind-shock models of X-ray production by extracting kinematic and spatial information from the line profiles. The profiles are Doppler broadened by the bulk motion of the hot plasma embedded in the highly supersonic wind. Our quantitative line-profile model allows us to derive an onset radius of shock-heated plasma and also, for the highest signal-to-noise lines, the terminal velocity of the X-ray emitting plasma. We use these quantities to test the predictions of numerical simulations of wind-shock X-ray production.

The paper is organized as follows: In the next section we describe the data and our sample of O stars taken from the *Chandra* archive. In §3 we describe our data analysis and modeling methodology including the line profile model, which was first introduced by Owocki & Cohen (2001), the line-profile fitting procedure, and the derivation of the mass-loss rate from an ensemble of line fits. In §4 we present our results, including mass-loss rate determinations for each star in our sample, and in §5 we conclude with a discussion of the implications of the line profile fitting results.

## 2 THE PROGRAM STARS

### 2.1 Observations

All observations reported on in this paper were made with *Chandra*'s High Energy Transmission Grating Spectrometer (HETGS) (Canizares et al. 2005). The HETGS has two grating arrays: the Medium and High Energy Gratings (MEG and HEG). The MEG has a resolution of 0.023 Å, while the HEG has a resolution of 0.012 Å, but lower sensitivity. We used the standard reduction procedure (CIAO 3.3 to 4.3) for most of the spectra, but for Cyg OB 8A, which is in a crowded field, care had to be taken to properly centroid the zeroth order spectrum of the target star, and we had to run a customized reduction procedure.

The observed spectra consist of a series of emission lines superimposed on a bremsstrahlung continuum. The lines arise from high ionization states: most lines are from helium-like or hydrogen-like ions from elements N through S, and the remainder come from iron L-shell transitions, primarily in Fe XVII. *Chandra* is sensitive in the wavelength range from 1.2 to 31 Å (0.4 to 10 keV). However, the shortest-wavelength line we are able to analyze in our sample stars is the Si XIV line at 6.182 Å and the longest is the O VII line at 21.804 Å. The spectra vary in quality and some suffer from significant interstellar attenuation at longer wavelengths. These two factors determine the number of lines we are able to fit in each star.

[1] Effectively single in the sense that there is no obvious wind-wind interaction X-ray emission.

### 2.2 The sample

We selected every O and early B star in the *Chandra* archive with a grating spectrum – see XATLAS (Westbrook et al. 2008) – that shows obviously wind-broadened emission lines, aside from $\zeta$ Pup and HD 93129A, which we have already analyzed (Cohen et al. 2010, 2011). We eliminated from our sample those stars with known magnetic fields that are strong enough to provide significant wind confinement (this includes $\theta^1$ Ori C and $\tau$ Sco) and we also excluded obvious colliding-wind binary X-ray sources, which are hard and variable (such as $\gamma^2$ Vel and $\eta$ Car). Some objects remaining in the sample are possible colliding wind binary X-ray sources. They are included because their line profiles do not obviously appear to deviate from the expectations of the embedded wind shock scenario, although we give special scrutiny to the fitting results for these stars in §4 (or §5?). We also exclude main sequence stars and giants with spectral type O9.5 and later, as these stars (including $\sigma$ Ori AB and $\beta$ Cru) have X-ray lines too narrow to be understood in the context of standard embedded wind shocks. We ended up including one B star, the supergiant $\epsilon$ Ori (B0 Ia). The sample stars and their important parameters are listed in Table 2.2.

## 3 MODELING AND DATA ANALYSIS METHODOLOGY

### 3.1 X-ray emission line profile model

We use the model of X-ray emission and absorption introduced by Owocki & Cohen (2001) (OC2001). The Owocki & Cohen model has the benefit of describing a general X-ray production scenario, making few assumptions about the details of the physical mechanism that leads to the production of shock-heated plasma in the wind. The model does assume that the cold, absorbing material in the wind and the hot, X-ray-emitting material both follow a $\beta$-velocity law of the form

$$v = v_\infty (1 - R_*/r)^\beta, \tag{1}$$

where $v_\infty$, the terminal velocity of the wind, usually has a value between 1500 and 3000 km s$^{-1}$. The $\beta$ parameter, derived from H$\alpha$ and UV lines, typically has a value close to unity. The model also assumes that the volume filling factor of X-ray emitting plasma, $f_{\rm v}$, is zero below some onset radius, $R_{\rm o}$, and is constant above $R_{\rm o}$. Our implementation of the X-ray line profile model optionally includes the effects of porosity (Oskinova et al. 2006; Owocki & Cohen 2006) and of resonance scattering (Leutenegger et al. 2007) on the individual line profile shapes. We explore both effects for a subset of stars in our sample.

The adjustable free parameters of the profile model are generally just the normalization, the parameter that describes the onset radius of X-ray production, $R_{\rm o}$, and a fiducial optical depth parameter, $\tau_*$, which we describe below. For a few high signal-to-noise lines, we allow $v_\infty$, the wind terminal velocity, to be a free parameter of the fit as well. The parameter $R_{\rm o}$ controls the widths of the line via the assumed wind kinematics represented by eqn. 1. Small values of $R_{\rm o}$ correspond to more X-ray production close to the star where the wind has a small Doppler shift, while large values of $R_{\rm o}$ indicate that most of the X-rays come from high Doppler shift regions in the outer wind. Hydrodynamic models show shocks developing about half a stellar radius above the surface of the star – albeit with some variation based on treatments of the line force parameters and of the lower boundary conditions in numerical simulations (Feldmeier et al. 1997; Runacres & Owocki 2002) – so we should expect $R_{\rm o}$ to be about 1.5 $R_*$.

The optical depth of the wind affects the blue shift and asymmetry of the line profile. The optical depth at a given location in the wind, and thus at a given wavelength, is proportional to the constant $\tau_*$, given by

$$\tau_* = \frac{\kappa \dot{\rm M}}{4\pi R_* v_\infty}. \tag{2}$$

This constant appears in the exact expression for the optical depth at any arbitrary point in the wind,

$$\tau(p,z) = \int_z^\infty \kappa \rho(r') {\rm d}z' = \tau_* \int_z^\infty \frac{R_* {\rm d}z'}{r'^2 (1 - R_*/r')^\beta}, \tag{3}$$

where $p, z$ are the usual cylindrical coordinates: the impact parameter, $p$, is the projected distance from the z-axis centered on the star and pointing toward the observer, and $r \equiv \sqrt{p^2 + z^2}$.The second equality arises from substituting the $\beta$-velocity law into the general equation for the optical depth and employing the mass continuity equation. The value of $\tau_*$ controls the degree of asymmetry and blue shift of each line profile. The profile is calculated from

$$L_\lambda \propto \int_{R_{\rm o}}^\infty \eta e^{-\tau} {\rm d}V, \tag{4}$$

where $\eta$ is the X-ray emissivity (which depends on $f_{\rm v}$), $\tau$ is calculated using eqn. 3, and the volume integral is performed over the entire wind above $r = R_{\rm o}$. In addition to scaling with the mass-loss rate, $\tau_*$ is proportional to $\kappa$, the atomic opacity, and is thus dependent on wavelength. Note that the atomic opacity is effectively constant across a given line profile but it varies from line to line. We discuss the wind opacity further in §3.3.

### 3.2 Fitting procedure

All model fitting was done in XSPEC (v12.3 to 12.6). We fit the positive and negative first order spectra simultaneously, but not coadded. Coadded spectra are shown in the figures for display purposes, however. When there were a significant number of counts in the HEG measurements of a given line, we included those data in the simultaneous fit. In most cases there were negligible counts in the HEG data and we fit only the MEG data. Because Poisson noise dominates these low-count *Chandra* data, we could not use $\chi^2$ as the fit statistic, and instead used the C statistic (Cash 1979). As with $\chi^2$, a lower C value indicates a better fit, given the same number of degrees of freedom. We assessed goodness-of-fit via Monte Carlo simulations of the distribution of the C statistic for each line fit. For placing confidence limits on model parameters, $\Delta C$ is equivalent to $\Delta\chi^2$ with a $\Delta C$ value of 1 corresponding to a 68 per cent confidence bound in one dimension (Press et al. 2007). We establish confidence bounds on the model parameters of interest one at a time, allowing other parameters to vary while establishing these bounds. There is generally a mild anti-correlation between $R_{\rm o}$ and $\tau_*$, so

**Table 1.** Properties of Program Stars

| Star | Spectral Type | $T_{\rm eff}$ (kK) | $R$ ($R_\odot$) | log $g$ (cm s$^{-2}$) | $v_\infty$ (km s$^{-1}$) | MEG counts | HEG counts | exposure time (ksec) |
|---|---|---|---|---|---|---|---|---|
| HD 93250 | O3.5 V | 46.0 | 15.9 | 3.95 | 3250 | 6169 | 2663 | 193.7 |
| 9 Sgr | O4 V | 42.9 | 12.4 | 3.92 | 3100 | 4530 | 1365 | 145.8 |
| HD 150136 | O5 III | 40.3 | 15.1 | 3.69 | 3400 | 8581 | 2889 | 90.3 |
| Cyg OB2 8A | O5.5 I | 38.2 | 27.0 | 3.56 | 2650 | 6575 | 1892 | 65.1 |
| HD 206267 | O6.5 V | | | | | 1516 | 419 | 73.5 |
| 15 Mon | O7 V | 37.5 | 9.9 | 3.84 | 2150 | 1621 | 393 | 99.8 |
| $\xi$ Per | O7.5 III | 35.0 | 14.0 | 3.50 | 2450 | 5603 | 1544 | 158.8 |
| $\tau$ CMa | O9 II | 31.6 | 17.6 | 3.41 | 2200 | 1300 | 311 | 87.1 |
| $\iota$ Ori | O9 III | 31.4 | 17.9 | 3.50 | 2350 | 4836 | 1028 | 49.9 |
| $\zeta$ Oph | O9 V | 32.0 | 8.9 | 3.65 | 1550 | 5911 | 1630 | 83.8 |
| $\delta$ Ori | O9.5 II | 30.6 | 17.7 | 3.38 | 2100 | 6144 | 1071 | 49.1 |
| $\zeta$ Ori | O9.7 Ib | 30.5 | 22.1 | 3.19 | 1850 | 11018 | 2496 | 73.4 |
| $\epsilon$ Ori | B0 Ia | 27.5 | 32.4 | 3.13 | 1600 | 6813 | 1474 | 91.7 |

we also examined the joint constraints on two parameters, adjusting the corresponding value of $\Delta C$ accordingly. Joint confidence limits are shown along with the best-fit models, for fits to the Fe XVII line at 15.014 Å for several sources with varying degrees of wind signatures in Fig. 1.

To account for the weak continuum under each emission line, we first fit a region around the line with a continuum model having a constant flux per unit wavelength. This continuum model was added to the line-profile model when fitting the line itself. The fitting was generally then done with three free parameters: $\tau_*$, $R_{\rm o}$, and a normalization factor. We fixed $\beta$ at 1, and $v_\infty$ at the value given in Table 2.2. A discussion of the effects of changing $\beta$ and $v_\infty$ as well as sensitivity to continuum placement, treatment of blends, and other aspects of our analysis can be found in Cohen et al. (2010). One additional effect we account for is the radial velocity of each star. This effect was only significant for $\xi$ Per, which has $v_r = 57$ km s$^{-1}$ (Hoogerwerf et al. 2001).

The hydrogen-like Ly$\alpha$ lines in the spectra consist of two blended lines with wavelength separations that are much smaller than the resolution of the *Chandra* gratings. We fit these lines with a single model centered at the emissivity-weighted average of the two wavelengths. In some cases, the strong lines are blended with weaker lines. If the blending is too severe to be modeled, as it is for the O VIII Ly$\beta$ line at 16.006 Å, we excluded the line from our analysis entirely. If the blended portion of the line could be omitted from the fit range without producing unconstrained[2] results, we simply fit the model over a restricted wavelength range. The Ne X Ly$\alpha$ line at 12.134 Å, for example, produces well-constrained results, even when its red wing is omitted due to blending. If lines from the same ion are blended, such as the Fe XVII lines at 16.780, 17.051, and 17.096 Å, we fit three models to the data simultaneously, constraining the $\tau_*$ and $R_{\rm o}$ values to be the same for all the lines in the blended feature. In the case of the aforementioned iron complex, we also constrained the ratio of the normalizations of the two lines at 17.096 and 17.051 Å, which share a common lower level, to the theoretically predicted value of 0.9 (Mauche et al. 2001) because the blending is too severe to be constrained empirically.

The helium-like complexes are among the strongest lines in many of the sample stars' spectra, but they are generally heavily blended. The forbidden-to-intercombination line intensity ratios are a function of the local mean intensity of the UV radiation at the location of the X-ray emitting plasma (Leutenegger et al. 2006). And so the spatial (and thus velocity) distribution of the shock-heated plasma affects both the line intensity ratios and the line profile shapes. We model these effects in tandem and fit all three line profiles, including the relative line intensities, simultaneously, as described in Leutenegger et al. (2006). In order to do this, we use UV fluxes taken from TLUSTY (Lanz & Hubeny 2003) model atmospheres appropriate for each star's effective temperature and log $g$ values, as listed in Table 2.2. This procedure generates a single $\tau_*$ value and a single $R_{\rm o}$ value for the entire complex, and where $R_{\rm o}$ affects both the line shapes and the $f/i$ ratios. We generally had to exclude the results for Ne IX due to blending with numerous irons lines.

### 3.3 Analyzing the ensemble of line fits from each star

To extract the mass-loss rate from a single derived $\tau_*$ parameter value, a model of the opacity of the cold, unshocked component of the wind is needed. Then, along with values for the wind terminal velocity and stellar radius, eqn. 2 can be used to derive a mass-loss rate for a given line. To derive a single mass-loss rate from an ensemble of emission lines, each with their own $\tau_*$ value, as we do here, the wavelength dependence of the $\tau_*$ values is assumed to follow the wavelength dependence of the atomic opacity, and eqn. 2 is solved for the best $\tau_*(\lambda)$. Although this correlation between $\tau_*(\lambda)$ and $\kappa(\lambda)$ was not noted in the initial analyses of *Chandra* grating spectra, it has recently been shown for the high signal-to-noise spectrum of $\zeta$ Pup that if all lines in the spectrum are considered – but blends that cannot be modeled are excluded – and a realistic model of the wavelength-dependent wind opacity is used, then the wavelength trend in the ensemble of $\tau_*$ values is consistent with the atomic

[2] Unconstrained in the sense that the $\Delta C$ criterion does not rule out significant portions of model parameter space.

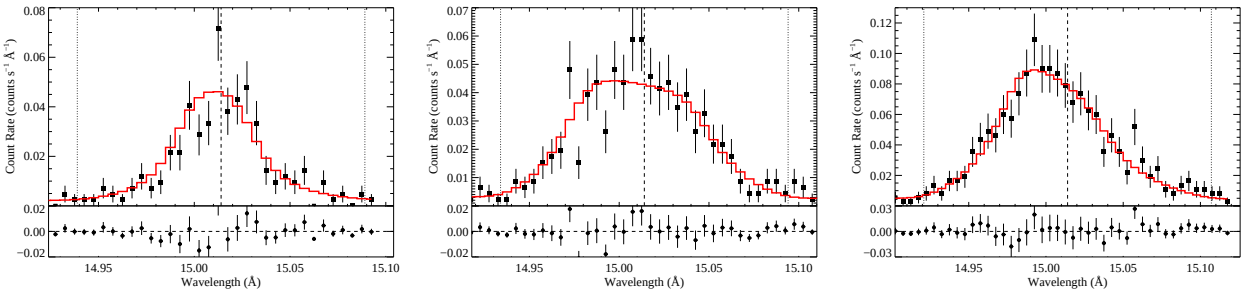


**Figure 1.** The Fe XVII line at 15.014 Å with best-fit model for three of the sample stars ($\zeta$ Oph, $\tau_* = 0.00^{+.01}_{-.00}$ (left), $\epsilon$ Ori, $\tau_* = 0.06^{+.10}_{-.06}$ (middle), and $\zeta$ Ori, $\tau_* = 0.38^{+.13}_{-.11}$ (right)) showing various degrees of asymmetry. The vertical dashed lines on the profile plots represent the laboratory line rest wavelength and the wavelengths corresponding to the terminal velocity of the wind.

opacity (Cohen et al. 2010). For other stars, the wavelength trend of $\tau_*$ expected from $\kappa(\lambda)$ may not be evident, but may still be consistent with it (as has been shown, recently, for HD 93129A (Cohen et al. 2011)).

The opacity of the bulk, unshocked wind is due to bound-free absorption (inner shell photoionization), and the contributions from N, O, and Fe are dominant, with important contributions from Ne and Mg at wavelengths below about 12 Å. The wind opacity is affected by the elemental abundances – both the overall metallicity and also the relative contributions of specific elements, most notably N and O, which are altered by CNO processing – and, to a lesser extent, by the ionization distribution in the wind.

In general, there do not exist precise abundance determinations for most of the stars in our sample, which are of course difficult to carry out and prone to systematic errors. The expectation is that these massive stars have metallicities close to solar, and that some, but not all, have enhanced nitrogen and depleted carbon and oxygen. Thus, we have calculated two generic wind opacity models: one using solar (Asplund et al. 2009) abundances and one that uses overall solar metallicity but has N at three times solar, O at 0.5 solar, and C at 0.25 solar. Note that the sum of the absolute C, N, and O abundances are, in this case, solar, even though the individual elemental abundances are not. We refer to these as the "solar" and "CNO processed" wind opacity models. Both assume an ionization balance based on O star models in (MacFarlane et al. 1994), but the opacity is largely insensitive to reasonable changes in the ionization distribution. We show these two opacity models in Fig. 2. Note that from 5 to 20 Å, the two models are nearly identical. At 20 Å, however, the oxygen K-shell edge is more apparent in the solar model than in the CNO-processed model. The only line that we are able to model longward of the oxygen edge is the O VII line complex near 21.7 Å. This complex is not strong in any of our sources, but with higher signal-to-noise data, it could be possible to use it to differentiate between the two opacity models, and even measure the nitrogen abundance in the wind.

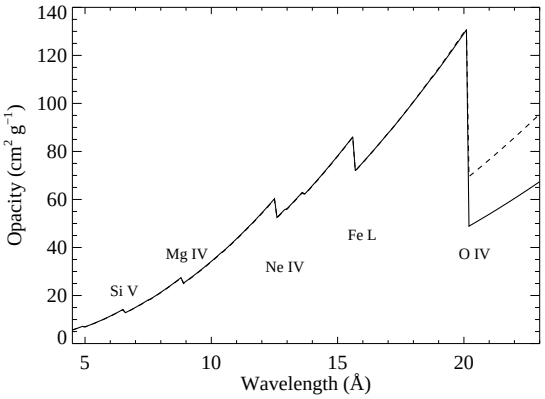


**Figure 2.** We present two different models for the wavelength-dependent opacity of the bulk wind, with the same simplified ionization balance assumed in each case, but altered C, N, and O abundances for the model shown as a dashed line. Prominent ionization edtes are labeled.

## 4 RESULTS

For each star in our sample, the simple line-profile model provides good fits to the emission lines and line complexes from which we are able to derive values for $\tau_*$ and $R_o$, using the formalism described in the previous section. In itself, this does not confirm the EWS scenario of X-ray production for each of the sample stars, as profile models with $\tau_* \approx 0$, at the spectral resolution of the *Chandra* gratings, are indistinguishable from a Gaussian, with the profile width controlled by the $R_o$ parameter. Rather, reasonable values of $\tau_*$ and $R_o$, and consistency between the $\tau_*$ values and the wavelength dependence of the atomic opacity of the wind are the minimum requirements to conclude that the EWS mechanism is operating in a given star and to interpret the ensemble $\tau_*$ values in the context of a mass-loss rate measurement.

There are three stars in the sample for which the data quality are not good enough to draw any meaningful conclusions: HD 206267, 15 Mon, and $\tau$ CMa. These are the three datasets with fewer than 2500 total MEG + HEG counts, and for none of these stars are there more than three emission lines for which profile fits with even marginal constraints can be made (and for none of the stars is there more than one weak line that is not potentially subject to resonance scattering and the associated ambiguity of model interpretation). We will not discuss these stars further in this paper. A fourth star, HD 93250, has only three usuable lines, although it has a significantly larger number of counts in its spectra than the three stars we are exclud-

ing. The small number of strong lines, despite the higher signal-to-noise spectra, can be understood in the context of the high plasma temperature and correspondingly strong bremsstrahlung continuum and weak lines in the HD 93250 spectra. As we discuss in the next section, this is a strong indication that the X-ray spectrum of HD 93250 is dominated by hard X-ray emission from colliding wind shocks in the context of the binary wind-wind interaction mechanism.

We summarize the fitted $\tau_*$ and $R_o$ values, and their uncertainties, in Figs. 3 and 4, respectively, and in Table 4. In these two figures, each point represents the fit to a single line or blended line complex. For $\epsilon$ Ori, we find that including the effects of resonance scattering is important for two lines, and in the corresponding panel of Fig. 3 we show two points for each of these lines, one representing the results with resonance scattering included and one without. There are a small number of lines for which the fits are only of marginal quality or which provide suspect results. These include the Si XIII complex in $\zeta$ Ori, for which the line shapes look unusually peaked and the formal upper limit on $\tau_*$ is remarkably small and a few of the Ne IX complexes, which are probably affected by blending with numerous iron lines[3] For $\delta$ Ori, there is some indication that the lines are mildly red-shifted (rather than the expected net blue shift due to wind absorption). This is likely due to binary orbital motion of the primary. We discuss this result for $\delta$ Ori, and the interpretation of the results for each individual star, in the following section.

From the ensemble of line-fit results for each star, we derive a mass-loss rate according the procedure outlines in §3.3, which we show graphically in each panel of Fig. 3, along with the trend of $\tau_*$ values expected from the theoretical mass-loss rate of each star. We also fit an average $R_o$ value for each star based on the ensemble of line-fit results. These average $R_o$ values are displayed graphically in each panel of Fig. 4. In all cases, the fitted $R_o$ values are consistent with a single, global value for each star, although for a small number of stars there is a hint of a correlation between $R_o$ and wavelength, although in no case is such a trend statistically significant. Again, the overall trends and results for each individual star are discussed in detail in the next section. Finally, for a few lines in some of the sample stars' spectra, we treat the wind terminal velocity, $v_\infty$, as a free parameter (as described in §3.2). These results are shown in Fig. 5 and listed in Table 4.

**Table 3.** Fit Results

| Star | Spectral Type | UV $v_\infty$ (km s$^{-1}$) | $v_\infty$ (km s$^{-1}$) |
|---|---|---|---|
| HD 93250 | O3.5 V | | |
| 9 Sgr | O4 V | | |
| HD 150136 | O5 III | | |
| Cyg OB2 8A | O5.5 I | | |
| $\xi$ Per | O7.5 III | | |
| $\iota$ Ori | O9 III | | |
| $\zeta$ Oph | O9 V | | |
| $\delta$ Ori | O9.5 II | | |
| $\zeta$ Ori | O9.7 Ib | | |
| $\epsilon$ Ori | B0 Ia | | |

## 5 DISCUSSION AND CONCLUSIONS

While the empirical line profile model provides good fits to nearly all the lines in all the sample stars, one of the primary results of this study is the overall weakness – or even absence – of wind absorption signatures in the *Chandra* grating spectra of O stars. This has been noted before by various authors examining individual objects, generally via fitting Gaussian profile models (e.g. Miller et al. (2002)), but here we have systematically quantified this result using a more physically meaningful line-profile model. There are three classes of explanations for the weak wind-absorption signatures we measure: (1) the line profile model is missing some crucial physics that masks the actual effects of wind absorption; (2) processes other than embedded wind shocks are contributing to the X-ray line emission and thereby diluting the characteristic shifted and skewed profiles that are the signature of wind absorption; and (3) the actual mass-loss rates of these stars are lower than expected.

Examining the trends in $\tau_*$ and $R_o$ shown in Figs. 3 and 4, we can identify several stars with extremely low wind optical depths and shock onset radii that deviate significantly from the expectations of the embedded wind shock scenario. These include HD 93250, HD 150136, iota Ori, zeta Oph, and delta Ori. As we show below, it is likely that nearly all of these stars, and also Cyg OB2 8A, have a significant contribution from colliding wind shocks in their observed X-ray line profiles. The other stars in the sample: 9 Sgr, xi Per, zeta Ori, and epsilon Ori have line profiles that are consistent with the expectations of the embedded wind shock scenario, with $R_o \approx 1.5\ R_*$ and $\tau_*$ values that, while low, are within an order of magnitude of the expected values and are consistent with the expected wavelength trend of the atomic opacity of their winds. The mass-loss rates we derive for these four stars from their ensembles of $\tau_*$ values are listed in Tab. 2 and are generally a factor of a few lower than the theoretical values computed by Vink et al. (2000). We summarize the X-ray-derived mass-loss rates for all the stars in the sample (even those for which the derived values cannot be trusted) in Fig. 6, and compare these mass-loss rates to the theoretical values. We also include $\zeta$ Pup and HD 93129A in this figure, as the X-ray line profiles of those two O supergiants were analyzed in earlier papers using the same techniques we employ here. We will discuss the results shown in this figure further, below, but first let us consider each star in our sample, with an eye toward differentiating among the three scenarios outlined above for explaining the weaker-than-expected line profile wind absorption signatures.

[3] Above temperatures of about 0.4 keV, the iron lines that interfere with the Ne IX measurement are particularly strong. *Co-authors: we have done some modeling of this temperature dependence – which should be broadly useful to people analyzing this complex in other objects – and we could even consider including a short appendix on this line complex and the blending issues in this paper.*

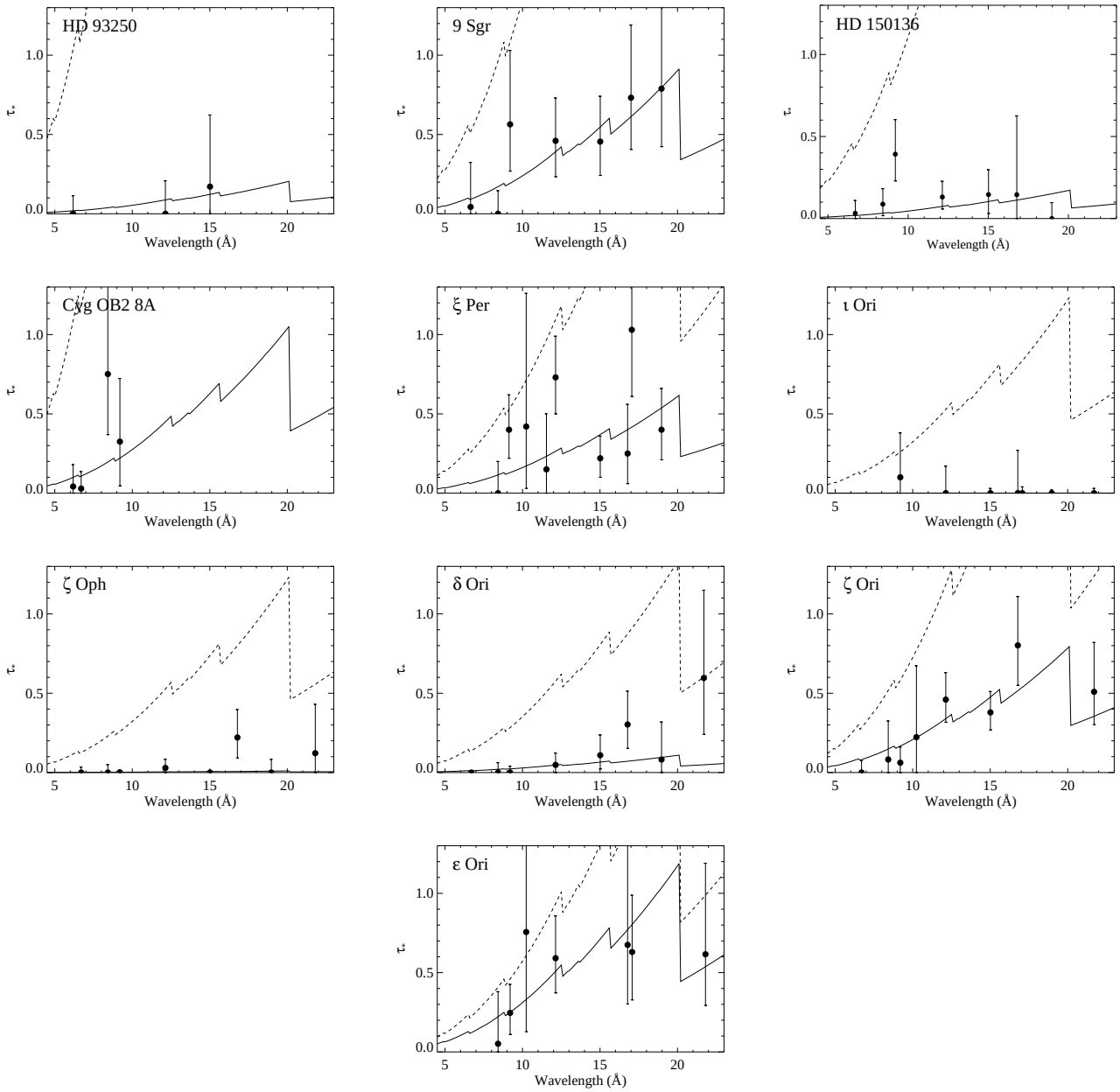


**Figure 3.** The fitted $\tau_*$ values (points), along with the 68 per cent confidence limits (error bars). The mass-loss rates derived from these values are shown graphically as the solid line, while the dashed line in each panel represents the $\tau_*$ trend expected from the theoretical mass-loss rates listed in Table 4. For $\epsilon$ Ori...

### 5.1 Individual stars

#### *5.1.1 HD 93250*

The *Chandra* grating spectrum of this early O main sequence star is quite hard and bremsstrahlung dominated, indicating that the spectral hardness is due to high plasma temperatures rather than being a by-product of wind and ISM absorption. The early O supergiant HD 93129A similarly has a hard X-ray spectrum, but in that star, the hardness is due almost entirely to high levels of wind and interstellar absorption (Cohen et al. 2011). HD 93250 was identified as being anomalous in X-rays in the recent Chandra Carina Complex Project (Townsley et al. 2011), with an X-ray luminosity even higher than that of HD 93129A, and a high X-ray temperature derived from low-spectral-resolution *Chandra* ACIS data (Gagné et al. 2011). Those authors suggest that the X-rays in HD 93250 are dominated by colliding wind shocks from interactions with an assumed binary companion having an orbital period greater than 30 days. Soon after the publication of that paper, Sana et al. (2011) announced an interferometric detection of a binary companion at a separation of 1.5 mas, corresponding to 3.5 AU. Thus it seems that the hard and strong X-ray spectrum and the symmetric and unshifted X-ray emission lines can be readily explained in the context of CWS X-ray emission.

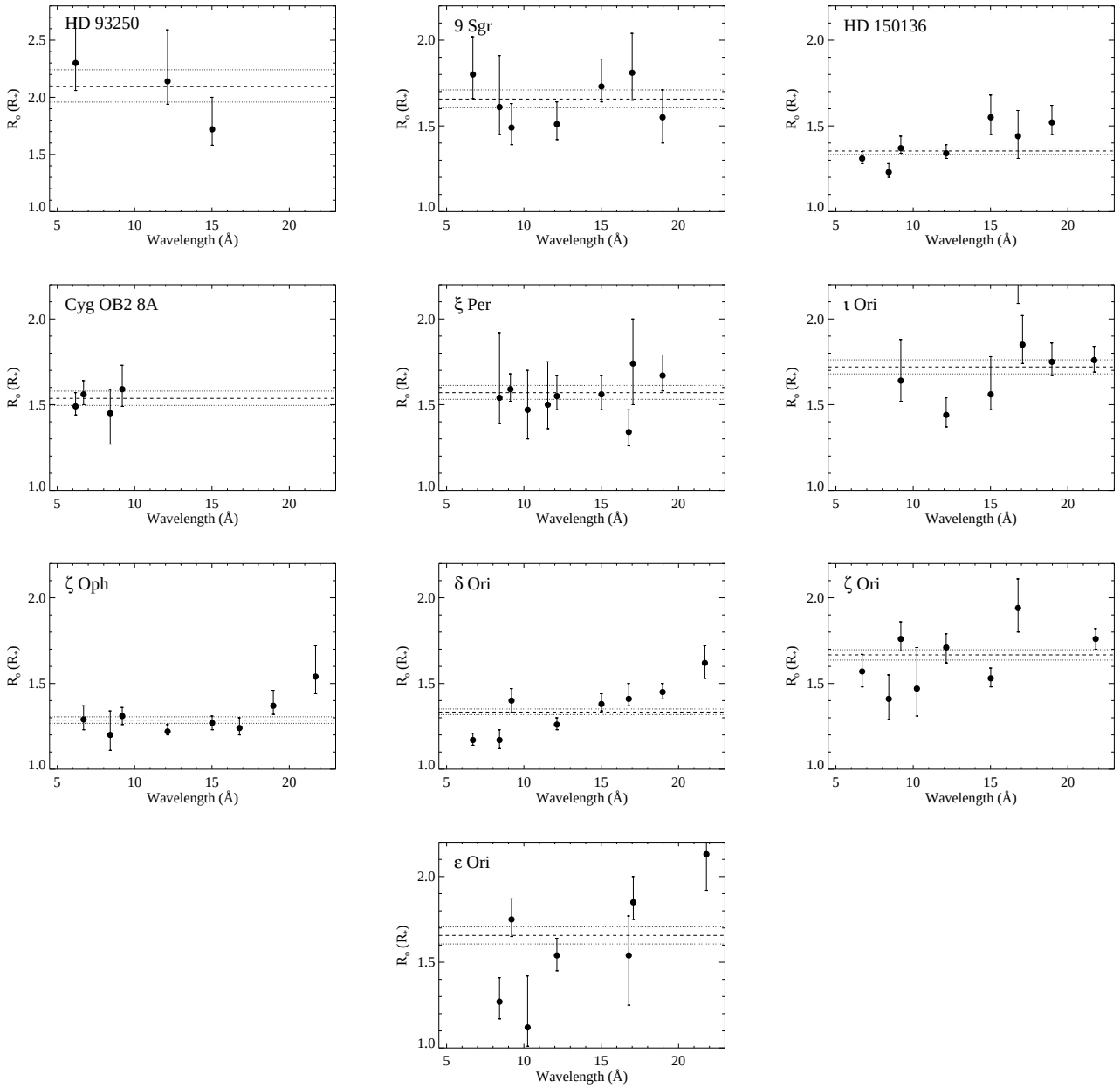


**Figure 4.** The fitted $R_{\rm o}$ values for each line in each sample star (points), along with the 68 per cent confidence limits (error bars). The best-fit global $R_{\rm o}$ value for each star is indicated in each panel by the dashed line, while the dotted lines indicate the extent of the 68 per cent confidence limits.

**Figure 5.** The fitted $v_\infty$ values, along with the 68 per cent confidence limits...

*5.1.2 9 Sgr*

This star is known to be a spectroscopic binary with a massive companion in an 8 or 9 year orbit (Rauw et al. 2005). The X-ray properties of 9 Sgr were described by Rauw et al. (2002) based on *XMM-Newton* observations. These authors noted blue-shifted line profiles, based on Gaussian fits, and also a somewhat higher than normal $L_{\rm X}/L_{\rm Bol}$ ratio and a moderate amount of hot ($T \approx 20$ MK) plasma based on fits to the *XMM-Newton* EPIC spectrum, although only about one per cent of the X-ray emission measure is due to this hot component. A simple CWS model computed by Rauw et al. (2002) shows that the observed X-ray emission levels cannot be explained by colliding wind shocks, and the authors conclude that the X-ray emission is dominated by embedded wind shocks. Presumably the separation of the components and/or their relative wind momenta are not optimal for producing CWS X-ray emission. It is reasonable to assume that while there may be a small amount of contamination from CWS X-rays, the line profiles we measure in the *Chandra*

**Table 2.** X-ray Derived Results for Each Star

| Star | Spectral Type | $\dot{M}_{\rm theory}$ ($M_\odot$ yr$^{-1}$) | $\dot{M}$ ($M_\odot$ yr$^{-1}$) | $R_{\rm o}$ ($R_*$) |
|---|---|---|---|---|
| HD 93250 | O3.5 V | $6.0 \times 10^{-6}$ | $1.2^{+1.5}_{-1.2} \times 10^{-7}$ | $2.09^{+.15}_{-.13}$ |
| 9 Sgr | O4 V | $2.1 \times 10^{-6}$ | $3.7^{+1.0}_{-0.9} \times 10^{-7}$ | $1.66^{+.05}_{-.05}$ |
| HD 150136 | O5 III | $2.3 \times 10^{-6}$ | $9.4^{+4.0}_{-4.1} \times 10^{-8}$ | $1.35^{+.02}_{-.02}$ |
| Cyg OB2 8A | O5.5 I | $8.7 \times 10^{-6}$ | $8.0^{+5.1}_{-5.1} \times 10^{-7}$ | $1.54^{+.04}_{-.04}$ |
| $\xi$ Per | O7.5 III | $9.3 \times 10^{-7}$ | $2.2^{+0.6}_{-0.5} \times 10^{-7}$ | $1.57^{+.05}_{-.04}$ |
| $\iota$ Ori | O9 III | $5.5 \times 10^{-7}$ | $3.2^{+84.}_{-3.2} \times 10^{-10}$ | $1.72^{+.04}_{-.04}$ |
| $\zeta$ Oph | O9 V | $1.8 \times 10^{-7}$ | $1.5^{+2.8}_{-1.5} \times 10^{-9}$ | $1.29^{+.02}_{-.02}$ |
| $\delta$ Ori | O9.5 II | $5.3 \times 10^{-7}$ | $4.3^{+2.6}_{-2.2} \times 10^{-8}$ | $1.33^{+.02}_{-.01}$ |
| $\zeta$ Ori | O9.7 Ib | $1.2 \times 10^{-6}$ | $3.4^{+0.6}_{-0.6} \times 10^{-7}$ | $1.67^{+.03}_{-.03}$ |
| $\epsilon$ Ori | B0 Ia | $1.2 \times 10^{-6}$ | $6.5^{+1.1}_{-1.5} \times 10^{-7}$ | $1.66^{+.05}_{-.05}$ |

grating spectra are dominated by the EWS mechanism, and therefore the mass-loss rate we derive from the profile fitting is indeed a good approximation to the true mass-loss rate. We note, also, that according to the radial velocity curve shown in Rauw et al. (2005) the *Chandra* grating spectrum we analyze in this paper was taken during a phase of the orbit when the primary's radial velocity was close to zero.

#### *5.1.3 HD 150136*

A well-known spectroscopic binary, with a period of only 2.662 days (Niemela & Gamen 2005), the HD 150136 system has previously been studied in the X-ray using the same data we reanalyze here (Skinner et al. 2005). Those authors find a very high X-ray luminosity but a soft spectrum with broad X-ray emission lines. They also detect some short period X-ray variability that they tentatively attribute to an occultation effect. Although colliding wind binaries with strong X-ray emission are generally thought to produce hard X-ray emission, it has recently been shown that many massive O+O binaries have relatively soft emission and modest X-ray luminosities, especially if their orbital periods are short (Gagné et al. 2011; Gagné 2012). We discuss the physics behind this in more detail below. And in any case, this star's X-ray emission stands out from the other giants and supergiants in the X-ray spectral morphology study of Walborn et al. (2009) by virtue of its high H-like/He-like silicon line ratio, indicating the presence of some hotter plasma. We conclude that although a few of the X-ray emission lines measured in this star's spectrum have non-zero $\tau_*$ values, overall the lines are too heavily contaminated by X-rays from colliding wind shocks to be used as a reliable mass-loss rate indicator.

#### *5.1.4 Cyg OB2 8A*

With phase-locked X-ray variability, a high $L_{\rm X}/L_{\rm Bol}$, and a significant amount of hot plasma with temperatures above 20 MK (De Becker et al. 2006), Cyg OB2 8A has X-ray properties characteristic of colliding wind shocks. It is a spectroscopic binary with a 21 day period in an eccentric orbit, and a semi-major axis of 0.3 AU. The small number of short-wavelength lines we are able to fit are not terribly inconsistent with the expectations of the embedded wind shock scenario, although the inferred mass-loss rate is roughly an order of magnitude lower than the theoretically expected value. However, because they are only present at short wavelengths, where the wind opacity is low, they do not provide very much leverage on the mass-loss rate, and are generally consistent with $\tau_* = 0$. We included this star in our sample because of prior analysis of the same Chandra grating data in the context of embedded wind shocks (Waldron et al. 2004), but given the thorough analysis by De Becker et al. (2006), we must conclude that the X-rays are dominated by colliding wind shocks, and the profile fits we present here do not provide information about embedded wind shocks or the wind mass-loss rate.

#### *5.1.5 $\xi$ Per*

A runaway star without a close binary companion and with constant radial velocity (Sota et al. 2008), $\xi$ Per should not have any binary colliding wind shock emission contaminating the X-ray emission lines we analyze. It does, however, show significant UV and H$\alpha$ variability, at least some of which is rotationally-modulated (De Jong et al. 2001). Thus the assumptions of spherical symmetry and a wind that is smooth on large scales is violated to some extent. Still, the X-ray line profiles should provide a relatively reliable mass-loss rate. The $\tau_*$ values we find are significantly larger than zero and are consistent with the expected wavelength trend. The mass-loss rate we derive is roughly a factor of five below the theoretic value from Vink et al. (2000).

#### *5.1.6 $\iota$ Ori*

Of all the stars in the sample, $\iota$ Ori shows the least amount of line asymmetry and blue shift, with all seven lines and line complexes we analyze having $\tau_*$ values consistent with zero. Taken at face value, the derived mass-loss rate is three orders of magnitude below the theoretical value. The derived $R_{\rm o}$ values are also unusual, being consistently higher than 1.5 $R_*$. The star is in a multiple system, with the closest component a spectroscopic binary in a highly eccentric, 29 day orbit (Bagnuolo et al. 2001). Although there are no definitive signatures of CWS X-ray emission (such as orbital modulation of the X-rays), it is very likely that the

quite broad but symmetric emission lines we have measured are from colliding, rather than embedded, wind shocks.

#### *5.1.7 ζ Oph*

This star also has a nearly complete lack of wind absorption signatures in its line profiles, as shown in Fig. 3. And its lines are narrower than expected in the EWS scenario, as shown by the low $R_o$ values in Fig. 4. Unlike the other stars in the sample with X-ray profiles that are difficult to understand in the context of embedded wind shocks, ζ Ori does not have a binary companion likely to produce colliding wind shock X-rays. It is, however, a very rapid rotator ($v \sin i = 351$ km s$^{-1}$ (Conti & Ebbets 1977)), goes through H$\alpha$ emission episodes that qualify it as an Oe star (Barker & Brown 1974), and has an equatorially concentrated wind (Massa 1995). The wind's deviation from spherical symmetry could explain the relatively symmetric and narrow X-ray emission lines, most likely through alterations to the line-of-sight velocity distribution of the emitting plasma in the wind. Detailed modeling, which is beyond the scope of this paper, would be required to place constraints on the degree of wind absorption in the X-ray lines in such a scenario.

#### *5.1.8 δ Ori*

With a quite small amount of wind attenuation evident in its line profiles and narrower than expected lines, the results from δ Ori are also suspect, although there are some emission lines with non-zero taustar values in its *Chandra* spectrum. This star is a member of a multiple system that includes an eclipsing, spectroscopic binary companion with an orbital period of 5.7 days. The companion is an early B star, and an earlier analysis of these same *Chandra* data indicated that colliding wind shocks were not likely to be strong enough to account for the X-ray luminosity of $L_X \approx 10^{32}$ ergs s$^{-1}$ (Miller et al. 2002). Given the uncertainty in the companion's wind properties as well as general uncertainties in the CWS model's X-ray emission predictions, it seems quite likely that a significant fraction of the observed X-ray line emission arises in the wind-wind interaction zone between the late O star and its early B companion, rendering the mass-loss rate we derive unreliable.

#### *5.1.9 ζ Ori*

Significant wind absorption signatures are seen in the X-ray profiles of ζ Ori, which has the highest signal-to-noise *Chandra* spectrum of any of the stars in our sample. The expected wavelength trend is seen in the $\tau_*$ results, and the fitted $R_o$ values are consistent with $R_o = 1.5\ R_*$, expected in the embedded wind shock scenario. While it is possible that there could be some contamination from CWS X-ray emission, the binary companion of ζ Ori is two magnitudes fainter than the primary and is at a separation of about 10 AU, making strong CWS emission an unlikely scenario (Hummel et al. 2000; Rivinius et al. 2011).

#### *5.1.10 ϵ Ori*

The only B star in our sample, ϵ Ori is a B0Ia MK standard, and given its evolved state and high luminosity, its wind is as strong as many of the O stars in our sample. Nearly all of the X-ray emission lines show wind signatures with $\tau_*$ values that deviate significantly from zero. It is also the only star in our sample for which eliminating the lines most likely subject to resonance scattering has a material effect on our derived mass-loss rate, increasing it from $2.1 \times 10^{-7}$ $M_\odot$ yr$^{-1}$ to $6.4 \times 10^{-7}$ $M_\odot$ yr$^{-1}$. Eliminating those lines also significantly improves the mass-loss rate fit to the $\tau_*$ values. And the low wind terminal velocity of ϵ Ori makes resonance scattering Sobolev optical depths larger, all things being equal, so the importance of the effect here, but not apparently in other stars, is reasonable. Thus, we report the higher mass-loss rate in Table 4 and show the fit from which that value is derived in Fig 3. There is no reason to believe that CWS X-ray emission affects the star's *Chandra* spectrum. Its only known companion is at 3′ (Halbedel 1985) (which is easily resolved by *Chandra*) but is not seen in the *Chandra* data, while interferometric observations show no binary companion down to small separations (Richichi & Percheron 2002).

### 5.2 Discussion

Taking the X-ray profile information we have analyzed here, along with knowledge of the multiplicity and other properties of the sample stars, it seems that at least half of the viable stars in the sample have some significant contamination of their X-ray profiles from colliding wind shock X-ray emission due to the interaction of their winds with those from binary companions. CWS X-ray emission is generally considered to be harder and stronger than that from embedded wind shocks, but that seems to be the case primarily in systems where both components have very strong winds with relatively closely matched wind momenta. Furthermore, systems with short periods often lack hard X-rays emission and the expected X-ray over-luminosity (Gagné 2012), and thus might not be immediately obvious as CWS-dominated systems based on a snapshot of their X-ray spectral energy distributions. Furthermore, while idealized CWS models predict distinctive X-ray emission line profile shapes (Henley et al. 2003), such shapes are not observed in real systems (e.g. Henley et al. (2005)), perhaps because of shock instabilities and the associated mixing and large random velocity components of the X-ray emitting plasma (Pittard & Parkin 2010). Therefore, when a mixture of CWS and EWS X-rays are present, the observed, hybrid line profiles should be relatively symmetric and broad, mimicking pure EWS profiles with little or no absorption.

The three earliest O stars in our sample where we suspect CWS X-ray contamination do in fact have X-ray properties that are quite different than normal O stars dominated by EWS X-ray emission. HD 93250, HD 150136, and Cyg OB2 8A are overluminous in the X-ray and/or have unusually hard X-ray emission. All three have O star binary companions with separations likely to lead to enhanced CWS X-ray emission. The later O stars where we suspect binary CWS contamination, ι Ori and δ Ori, have overall X-ray emission levels and temperatures that are not far out of line

with those expected from EWS sources. But they do have close, massive binary companions and X-ray line properties that are inconsistent with a purely EWS origin. It is possible that they are only partially contaminated by CWS emission (perhaps this is the case, too, for HD 150136, where some of the X-ray emission lines also show non-zero taustar values).

While the five stars mentioned in the previous paragraph all seem to fall into case (2) enumerated in the opening paragraph of this section – contamination of the observed X-rays by a process other than the EWS mechanism – the other object with results difficult to interpret in the EWS framework based on our line profile model fits likely falls into case (1), a breakdown of the assumptions in our simple X-ray line profile model. That object is $\zeta$ Oph, for which there is strong evidence for a non-spherical wind. Because the line profile model we employ assumes spherical symmetry and the resulting geometry and kinematics governs the manifestation of wind attenuation in the line profiles, we cannot interpret the derived taustar values in terms of wind attenuation for this star.

The remaining stars in the sample: 9 Sgr, $\xi$ Per, $\zeta$ Ori, and $\epsilon$ Ori have X-ray profiles that are consistent with the expectations of the EWS scenario, with significant wind attenuation evident from the fitted taustar values, which also show the expected wavelength trend of longer-wavelength lines having larger optical depths due to the greater wind opacity at those wavelengths. These stars have fitted $R_{\rm o}$ values of $R_{\rm o} \approx 1.5\ R_*$, confirming the predictions of LDI simulations of embedded wind shocks (Feldmeier et al. 1997; Runacres & Owocki 2002). We note also that there is no strong evidence for a wavelength trend in the derived $R_{\rm o}$ values for these stars. For each star, the shock onset radius is consistent with a single value, although there are hints of a positive correlation between $R_{\rm o}$ and wavelength for $\epsilon$ Ori. Additionally, for each of these four stars, we fit some of the stronger lines with models for which we allowed the wind terminal velocity, $v_\infty$, to be a free parameter. In each case, we find values consistent with the terminal velocities of their bulk, UV absorbing winds. This confirms the predictions of LDI simulations which show that the shocked wind plasma is typically moving at roughly the same speed as the ambient, unshocked wind.

The mass-loss rates we derive from fitting the ensemble of $\tau_*$ values for each star are listed in Table 4, where we also compare them to theoretical mass-loss rates from Vink et al. (2000). We summarize these results and comparisons in Fig. 6, which graphically compares the theoretical and X-ray profile mass-loss rates. We also include $\zeta$ Pup and HD 93129A in this figure, as we derived mass-loss rates from X-ray profiles for those stars in earlier papers using the same methodology we employ here. In addition, we include the other six sample stars in that figure to show the extent to which they are outliers. While Cyg OB2 8A's X-rays are surely dominated by CWS emission, because the only lines we can analyze are at short wavelengths where the wind opacity is low, the X-ray based mass-loss rate for that star is not extremely low compared to theory. The stars $\delta$ Ori and HD 150136 have X-ray based mass-loss rate determinations only an order of magnitude lower than theoretical predictions, indicating that there could be some contribution to the observed emission lines from EWS X-rays. The X-ray mass-loss rates of HD 93250, $\iota$ Ori, and $\zeta$ Oph are very low, however, indicating significant wind contamination or non-spherical wind geometry in those objects. Of the four stars in this study with reliable X-ray mass-loss rates and the two from previous studies, we find mass-loss rates that range from being slightly less than theoretical predictions ($\epsilon$ Ori, $\zeta$ Pup, HD 93129A) to about six times less (9 Sgr, $\xi$ Per, and $\zeta$ Ori).

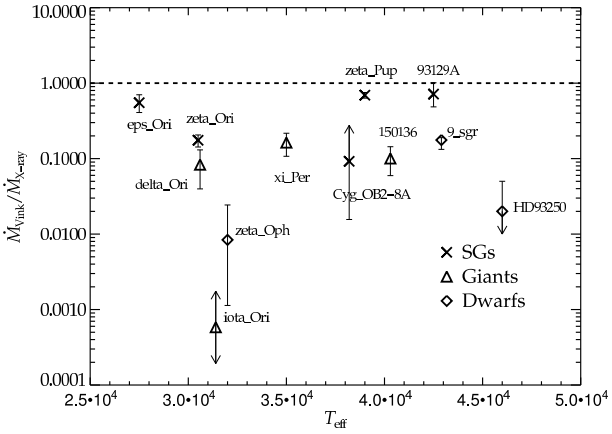


**Figure 6.** The X-ray derived mass-loss rates for each star in our sample (and also $\zeta$ Pup and HD 93129A) expressed as a ratio of the theoretically expected mass-loss rates.

**ACKNOWLEDGMENTS**

Support for this work was provided by the National Aeronautics and Space Administration through *Chandra* award numbers AR7-8002X and AR0-11002B to Swarthmore College. EEW was supported by a Lotte Lazarsfeld Bailyn Summer Research Fellowship from the Provost's Office at Swarthmore College. JOS and SPO acknowledge support from NASA award ATP NNX11AC40G to the University of Delaware.

**REFERENCES**

Asplund M., Grevesse N., Sauval A. J., Scott P., 2009, ARAA, 47, 481
Bagnuolo W. G., Riddle R. L., Gies D. R., Barry D. J., 2001, ApJ, 554, 362
Barker P. K., Brown T., 1974, ApJ, 192, L11
Bouret J. C., Lanz T., Hillier D. J., 2005, A&A, 438, 301
Canizares C. R., et al., 2005, PASP, 117, 1144
Cash W., 1979, ApJ, 228, 939
Cassinelli J. P., Miller N. A., Waldron W. L., MacFarlane J. J., Cohen D. H., 2001, ApJ, 554, L55
Cohen D. H., Gagné M., Leutenegger M. A., MacArthur J. P., Wollman E. E., Sundqvist J. O., Fullerton A. W., Owocki S. P., 2011, MNRAS, 415, 3354
Cohen D. H., Kuhn M. A., Gagné M., Jensen E. L. N., Miller N. A., 2008, MNRAS, 386, 1855
Cohen D. H., Leutenegger M. A., Wollman E. E., Zsargó J., Hillier D. J., Townsend R. H. D., Owocki S. P., 2010, MNRAS, 405, 2391
Conti P. S., Ebbets D., 1977, ApJ, 213, 438
De Becker M., Rauw G., Sana H., Pollock A. M. T., Pittard J. M., Blomme R., Stevens I. R., van Loo S., 2006, MNRAS, 371, 1280
de Jong J. A., et al., 2001, A&A, 368, 601
Feldmeier A., Puls J., Pauldrach A. W. A., 1997, A&A, 322, 878
Fullerton A. W., Massa D. L., Prinja R. K., 2006, ApJ, 637, 1025
Gagné M., et al., 2011, ApJS, 194, 5
Gagné M., 2012, (arXiv:)
Halbedel E. M., 1985, PASP, 97, 434
Hamann W.–R., Feldmeier A., Oskinova L. M., 2008, Clumping in Hot Star Winds. Universitatsverlag, Potsdam
Henley D. B., Stevens I. R., Pittard J. M., MNRAS, 346, 773
Henley D. B., Stevens I. R., Pittard J. M., MNRAS, 356, 1308
Hoogerwerf R., de Bruijne J. H. J., de Zeeuw P. T., 2001, A&A, 365, 49
Hummel C. A., White N. M., Elias N. M., Hajian A. R., Nordgren T. E., 2000, ApJ, 540, L91
Kahn S. M., Leutenegger M. A., Cottam J., Rauw G., Vreux J.–M., den Boggende A. J. F., Mewe R., Güdel M., 2001, A&A, 365, L312
Lanz T., Hubeny I., 2003, ApJS, 146, 417
Leutenegger M. A., Cohen D. H., Sundqvist J. O., Owocki S. P., 2012, MNRAS, submitted
Leutenegger M. A., Owocki S. P., Kahn S. M., Paerels F. B. S., 2007, ApJ, 659, 642
Leutenegger M. A., Paerels F. B. S., Kahn S. M., Cohen D. H., 2006, ApJ, 650, 1096
MacFarlane, J. J., Cohen D. H., Wang P., 1994, ApJ, 437, 351
Mauche C. W., Liedahl D. A., Fournier M. B., 2001, ApJ, 560, 992
Massa D., 1995, ApJ, 438, 376
Miller N. A., Cassinelli J. P., Waldron W. L., MacFarlane J. J., Cohen D. H., 2002, ApJ, 577, 951
Niemela V. S., Gamen R. C., 2005, MNRAS, 356, 974
Oskinova L., Feldmeier A., Hamann W.–R., 2006, MNRAS, 372, 313
Owocki S. P., Cohen D. H., 2001, ApJ, 559, 1108
Owocki S. P., Cohen D. H., 2006, ApJ, 648, 565
Pittard J. M., Parkin E. R., 2010, MNRAS, 403, 1657
Press W. H., Flannery B. P., Teukolsky S. A., Vetterling W. T., 2007, Numerical Recipes, $3^{rd}$ edition. Cambridge University Press, Cambridge
Puls J., Markova N., Scuderi S., Stanghellini C., Taranova O. G., Burnley A. W., Howarth I. D., 2006, A&A, 454, 625
Rauw G., Sana H., Gosset E., De Becker M., Arias J., Morrell N., Eenens P., Stickland D., 2005, in "Massive Stars and High-Energy Emission in OB Associations," eds. G. Rauw, Y. Nazé, R. Blomme, & E. Gosset, Liege: JENAM, 85
Rauw G., Blomme R., Waldron W. L., Corcoran M. F., Pittard J. M., Pollock A. M. T., Runacres M. C., Sana H., Stevens I. R., Van Loo S., 2002, A&A, 394, 993
Repolust T., Puls J., Herrero A., 2004, A&A, 415, 349
Richichi A., Percheron I., 2002, A&A, 386, 492
Rivinius T., Hummel C. A., Stahl O., 2011, IAUS, 272, 539
Runacres M. C., Owocki S.P., 2002, A&A, 381, 1015
Sana H.., Le Bouquin J.-B., De Becker M., Berger J.-P., de Koter A., Mérand A., 2011, ApJ, 740, L43
Skinner S. L., Zhekov S. A., Palla F., Barbosa C. L. D. R., 2005, MNRAS, 361, 191
Skinner S. L., Sokal K. R., Cohen D. H., Gagné M., Owocki S. P., Townsend R. D., 2008, ApJ, 683, 796
Sota A., Maíz Apellániz J., Walborn N. R., Shida R. Y., 2008, Rev. Mex., 33, 56
Stevens I. R., Blondin J. M., Pollock A. M. T., 1992, ApJ, 386, 265
Sundqvist J. O., Owocki S. P., Cohen D. H., Leutenegger M. A., Townsend R. H. D., 2012, MNRAS, 420, 1553
Townsley L., et al., 2011, ApJS, (arXiv:1102.4779)
Vink J., de Koter A., Lamers H. J. G. L. M., 2000, A&A, 362, 295
Walborn N. R., Nichols J. S., Waldron W. L., 2009, ApJ, 703, 633
Waldron W. L., Cassinelli J. P., Miller N. A., MacFarlane J. J., Reiter J. C., 2004, ApJ, 616, 542
Westbrook O. W., et al., 2008, ApJS, 176, 218